Enhanced interfacial compatibility of FeS@N,S-C anode with ester-based electrolyte enables stable sodium-ion full cells

Jiyu Zhang [a], Zhen Meng [b], Dan Yang [a], Keming Song [a], Liwei Mi [c], Yunpu Zhai [a], Xinxin Guan [a], Weihua Chen [a,*]

[a] College of Chemistry, Zhengzhou University, Zhengzhou 450001, Henan, China
[b] Helmholtz Institute Ulm (HIU) Electrochemical Energy Storage, Ulm D-89081, Germany
[c] Centre of Advanced Materials Research, Zhongyuan University of Technology, Zhengzhou 450007, Henan, China

ARTICLE INFO

Keywords:
Sodium-ion batteries
Interfacial compatibility
Full cell
Electrolyte
Solid electrolyte interphase (SEI)

ABSTRACT

The development of sodium-ion full cells is seriously suppressed by the incompatibility between electrodes and electrolytes. Most representatively, high-voltage ester-based electrolytes required by the cathodes present poor interfacial compatibility with the anodes due to unstable solid electrode interphase (SEI). Herein, FeS@N,S-C (spindle-like FeS nanoparticles individually encapsulated in N,S-doped carbon) with excellent structural stability is synthesized as a potential sodium anode material. It exhibits exceptional interfacial stability in ester-based electrolyte (1 M $NaClO_4$ in ethylene carbonate/propylene carbonate with 5% fluoroethylene carbonate) with long-cycling lifespan (294 days) in Na|FeS@N,S-C coin cell and remarkable cyclability in pouch cell (capacity retention of 82.2% after 170 cycles at 0.2 A g^{-1}). DFT calculation reveals that N,S-doping on electrode surface could drive strong repulsion to solvated Na^+ and preferential adsorption to ClO_4^- anion, guiding the anion-rich inner Helmholtz plane. Consequently, a robust SEI with rich inorganic species (NaCl and Na_2O) through the whole depth stabilizes the electrode–electrolyte interface and protects its integrity. This work brings new insight into the role of electrode's surface properties in interfacial compatibility that can guide the design of more versatile electrodes for advanced rechargeable metal-ion batteries.

1. Introduction

Rechargeable sodium-ion batteries (SIBs) offer an excellent solution to electrochemical energy storage, especially in grid storage stations [1–3]. However, enormous obstacles remain in the way of their commercialization. One of the most critical challenges is poor compatibility between anode and electrolyte [4,5]. As an essential part, cathode materials have been studied widely and achieved encouraging performance in ester-based electrolytes, including transition metal oxides, NASICON-type material and Prussian blue analogues [6–11]. Unfortunately, most of the anode materials currently studied demonstrate poor electrochemical behaviour in ester-based electrolytes, with continuous electrolyte decomposition and reckless SEI growing, eventually causing the failure of cells [12,13]. To overcome this obstacle, pre-activation of cathode and anode in their respective electrolytes before the assembly of full cells is required, though it is complex and time-consuming [14].

Recently, considerable efforts have been attempted to build a stable anode-electrolyte interface. Taking into the role of electrolyte account, most of them have aimed at regulating electrolyte components and additives [15–19]. For example, salt-concentrated electrolytes have been developed to induce inorganic-rich SEI to stabilize anode [20]. Various electrolyte additives, such as fluoroethylene carbonate (FEC) and vinylene carbonate (VC), also play positive roles in building a high-quality SEI [21,22]. Given that the properties of the interface between anode and electrolyte are closely related to the potential, structure and chemical elements of the electrode surface [23–27], deep understanding of the intrinsic surface effect and targeted design of electrode materials are desired to promote the compatibility between electrode and electrolyte.

High-capacity iron sulfide anode, which is non-toxic and consists of earth-abundant elements, is promising to satisfy the demands for large-scale applications [28,29]. To improve the electric conductivity, suppress the large volume change and restain the

* Corresponding author.
E-mail address: chenweih@zzu.edu.cn (W. Chen).

polysulfides shuttle of iron sulfide during charge/discharge process, rational structural design of the material is introduced, e.g. carbon coating, nitrogen and sulphur-doping [30,31]. All these aspects should be considered for the reliable stability of electrodes [32–34]. Although FeS materials have been widely reported in ester-based electrolytes [35,36], their compatibility problems have not been revealed well, let alone designing effective material properties to enable improved interfacial stability.

Herein, FeS@N,S-C material with nano-sized FeS uniformly encapsulated into N,S-doped carbon matrix was fabricated, affording rich cavities in bulk and excellent structural stability. The structure and components of SEI that determines the interfacial stability in various electrolytes are demonstrated. DFT calculation was used to study the interfacial interactions between the electrode surface and various Na^+ solvation structures. Impressively, it is verified that the N,S-doping on the surface could guide partial exclusion to the solvated Na^+ and enhanced adsorption to ClO_4^- anions in $NaClO_4$ EC/PC electrolyte (1 M ethylene carbonate (EC)/propylene carbonate (PC) with 5% fluoroethylene carbonate (FEC)), which induces a durable inorganic-rich SEI. Such a highly stable SEI ensures a superb FeS@N,S-C electrode with long-lifespan cycling (294 days) in the coin cell and high cycling stability in the pouch cell.

2. Results and discussion

FeS@N,S-C is prepared through a homogeneous carbothermal reduction process from a precursor (Fig. S1) comprising $FeSO_4{\cdot}7H_2O$, L-cysteine and citric acid (Fig. 1a). X-ray diffraction pattern (XRD) demonstrates pure FeS phase with the lattice parameters of a, b = 5.9268 Å, c = 11.3817 Å, V = 346.24 Å^3 and a good weighted profile R-factor (R_p = 6.03%, Fig. 1b). The morphology of FeS@N,S-C was confirmed by transmission electron microscopy (TEM) and high-angle annular dark field-scanning transmission electron microscopy (HAADF-STEM) images. High-density FeS nanoparticles are highly dispersed in the carbon matrix (Fig. 1c), leaving a rough surface with bulgy particles (Fig. S2a–d). Most FeS nanoparticles show a length varying from 33 to 49 nm and a width ranging from 7 to 17 nm (Fig. 1d and Fig. S2e). The lattice fringes with interplanar spacings of 0.2883 and 0.2023 nm in Fig. 1(e) correspond to the (110) and (114) lattice planes of FeS, respectively, in good agreement with the result of corresponding fast-Fourier transformation (FFT) patterns and selected-area electron diffraction (SAED) (Fig. S2f). Some small FeS particles (~10 nm) with clear diffraction spots are also tightly embedded in carbon matrix (Fig. 1f). The carbon matrix effectively prevents the agglomerations of FeS particles during charge–discharge cycles and ensures good electronic conductivity [37]. Furthermore, the gas from the thermal decomposition of the precursor may result in a porous structure in the composite (Fig. 1g) [38]. N_2 adsorption–desorption measurement implies a mesoporous structure (Fig. S3). Abundant internal pores allow sufficient electrolyte inflation and reserved space for buffering volume change of the electrode, helping to relieve the internal stress in FeS@N,S-C electrode during sodiation/desodiation process [35,39].

The carbon structure in FeS@N,S-C is further investigated by various characterizations. Raman spectrum shows two distinct peaks around 1342 and 1570 cm^{-1}, representing sp^3-type disordered carbon (D band) and sp^2-type graphitized carbon (G band) [39], respectively (Fig. S4a). The I_D/I_G ratio of 1.93 suggests a highly defective degree. X-ray photoelectron spectroscopy (XPS) spectrum shows clearly three N species peaks, including pyridinic-N (398.1 eV), pyrrolic-N (399.9 eV) and graphitic-N (401.7 eV) (Fig. S4b) [3]. S 2p spectrum is primarily fitted to the C-S bond and S^{2-}, as validated by the peaks at 163.3 and 161.3 eV, with a part of oxidized group SO_x (Fig. S4c) [38]. Elemental mapping images show the distribution of Fe, S, N and C elements and indicate the well-dispersed FeS particles (Fig. 1h). Except for the localization of S in the particles, S and N elements are also highly distributed in the carbon matrix owing to their successful doping. Thermogravimetric analysis indicates the carbon content in FeS@N,S-C is around 10.5 wt% (Fig. S4d). The N and S contents (N/C = 0.1164, S/C = 0.0403, at%) are confirmed by element analysis (Table S1).

The electrochemical process of FeS@N,S-C electrode in various electrolytes is investigated through cyclic voltammetry (CV, Fig. 2a), including $NaClO_4$ EC/PC, $NaCF_3SO_3$ EC/PC (1 M $NaCF_3SO_3$ in EC/PC), $NaClO_4$ DGM (1 M $NaClO_4$ in diglyme) and $NaCF_3SO_3$ DGM (1 M $NaCF_3SO_3$ in DGM). The four electrolytes are supplemented with 5 wt% FEC additives. In $NaClO_4$ EC/PC electrolyte, a broad cathodic peak centered at 0.43 V arises due to the formation of SEI and the FeS's sodiation, which overlap [40]. During the anodic scans, the oxidation peak around 1.52 V corresponds to the formation of Na_xFeS [41]. In $NaCF_3SO_3$ EC/PC electrolyte, a sluggish SEI formation process is reflected by a broad cathodic peak from 0.01 to 0.81 V [42]. The voltage slope near 0.8–1.0 V is the characteristic of FEC's decomposition [43]. For DGM-based electrolytes, the decomposition of FEC shows a weak cathodic peak around 1.04 V, and the sharper cathodic peaks indicate a faster reaction kinetics process closely related to the remarkably reduced Na^+ desolvation barrier [44].

Cycling stability of FeS@N,S-C is evaluated via galvanostatic charge–discharge test (Fig. 2b), where its discharged capacities based on the mass of FeS are 607 ($NaClO_4$ EC/PC), 560 ($NaCF_3SO_3$ EC/PC), 664 ($NaClO_4$ DGM), 697 ($NaCF_3SO_3$ DGM) mAh g^{-1} upon the initial cycle, respectively. For comparison, extremely low capacities delivered by N,S-C electrodes suggest their negligible capacity contributions in FeS@N,S-C electrode (Fig. S5). Low initial coulombic efficiency (ICE) of FeS@N,S-C electrodes indicate a large amount of electrolyte decomposition caused by highly defective surface (Fig. S6) [31]. Nevertheless, in $NaClO_4$ EC/PC electrolyte, CE rapidly increased to 98.9% in the second cycle and maintained 99.54% of average CE in the following cycles, revealing a stable SEI and excellent structure stability during repeated (de)sodiation process. While the CE in the other three electrolytes show larger fluctuation with the average CE of 99.50%, 102.42% and 571.03%, respectively, and earlier over-charging originated from poor SEI, accompanied with larger voltage polarization [45]. Additionally, FeS@N,S-C achieves long-cycling stability in this electrolyte. The discharged capacity retains 205 mAh g^{-1} after 2450 cycles (294 days) with a capacity decay of 0.0199% per cycle (Fig. 2c). Notably, long-term cycling at low current density puts forward higher requirements on the structure and interface of the electrode. Therefore, this stresses the excellent stability of FeS@N,S-C electrode. Under high mass loading (4.24 mg cm^{-2}) or high rates, FeS@N,S-C electrode still exhibits remarkable reversibility and reliable repeatability (Fig. S7). When removing FEC additive from the electrolytes, improved ICE but terrible cycle stability appears (Fig. S8), which implies that FEC, as an introduced film-formation additive, plays an important role in improving batteries' cycling performance. However, unstable CE and poor capacity retention are still presented in $NaCF_3SO_3$ EC/PC and DGM-based electrolytes after dozens of cycles, suggesting that other dominant factors except FEC benefit the improved cycling stability of FeS@N,S-C electrode in $NaClO_4$ EC/PC electrolyte.

More importantly, benefited from superior interface stability in $NaClO_4$ EC/PC electrolyte, FeS@N,S-C can be directly utilized as an anode to match with commercial $NaFe_{1/3}Ni_{1/3}Mn_{1/3}O_2$ cathode (Fig. S9a–d), which can light up 49 light-emitting diodes (LED, Fig. 2d). Without pre-activation of cathode or anode in their preferable electrolytes, the assembled pouch cell exhibits a reversible

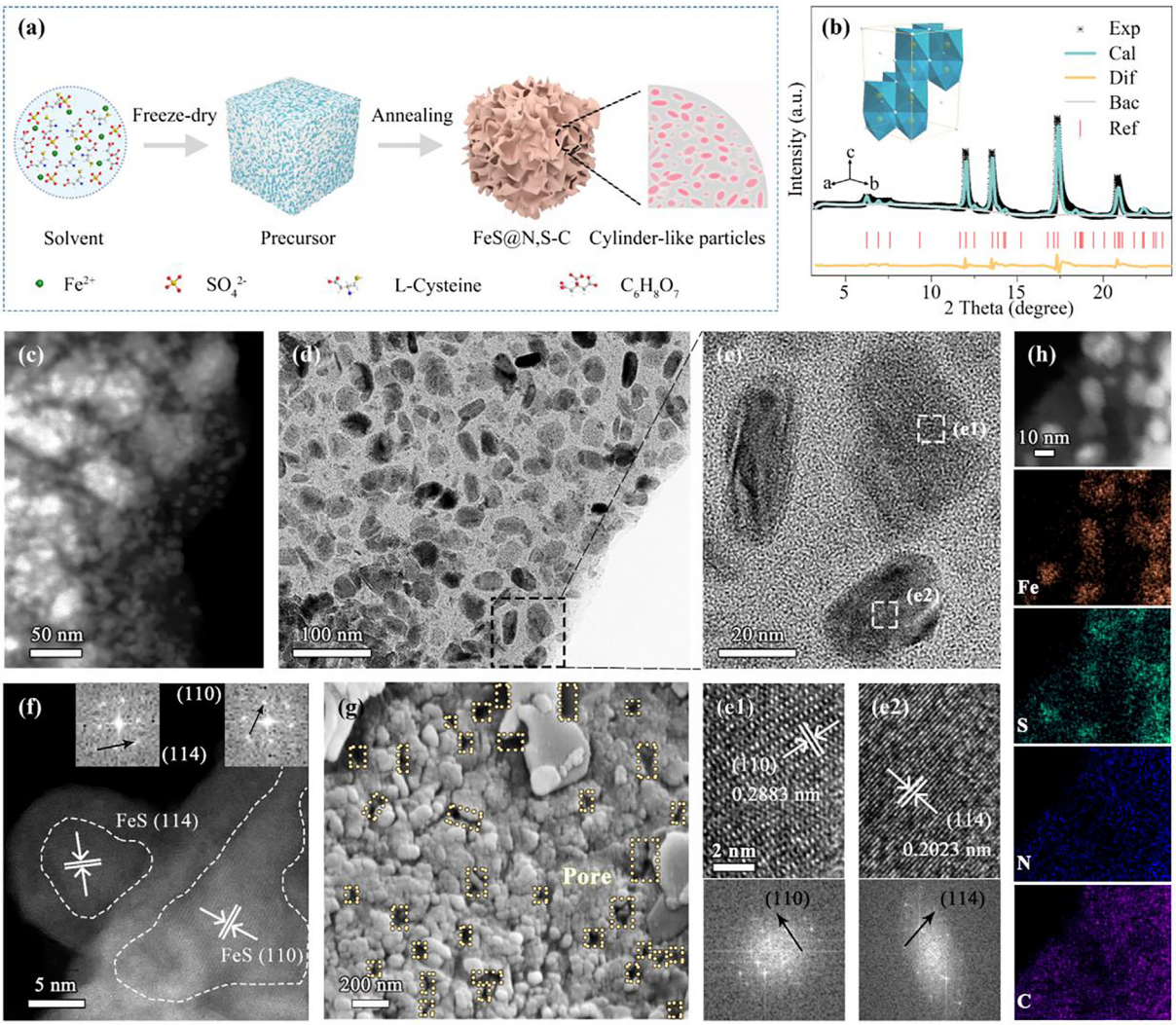

Fig. 1. Characterizations of as-synthesized FeS@N,S-C material. (a) Schematic diagram of the synthesis process. (b) Synchrotron high-pressure powder X-ray diffraction riveted refinement with the corresponding crystal structure. (c and f) HAADF-STEM images with FFT patterns. (d and e) TEM images. (e1 and e2) The enlarged TEM images with corresponding FFT patterns in two regions of (e). (g) SEM image from the cross-section. (h) Element distributions.

capacity of 301 mAh g^{-1} at 0.2 A g^{-1} (Fig. 2e) and remarkable capacity retention of 82.2% over 170 cycles (Fig. 2f). Meantime, a stable average CE around 99.43% after the initial cycles implies little electrolyte consumption, displaying high cycling reversibility and potential application prospects [46,47]. Furthermore, the low ICE of pouch cell can be effectively enhanced via pre-activation of the electrodes (Fig. S9e and f).

To find out the reason for the enhanced electrochemical performance of FeS@N,S-C electrode in the optimized electrolyte, *in-situ* and *ex-situ* XRD patterns are actualized upon the initial cycle (Fig. S10). The peak intensities at 29.8 ° and 33.9 ° in *in-situ* XRD patterns decrease and vanish at about 0.7 V upon the sodiation process, conforming to the insertion of Na^+ into FeS [38]. With the discharge proceeding, the Na_2S peak at 39.4 ° intensifies, which then decreases during the charging process. When charged to 2.5 V, the reappeared (110) and (112) diffraction peaks indicate the recovery of FeS phase. *Ex-situ* XRD patterns show similar change and more apparent Na_2S and Fe peaks, suggesting the intercalation reaction combined with conversion reaction of FeS@N,S-C during the charge–discharge process, consistent with that of FeS@C in the ether-based electrolyte (1 M $NaCF_3SO_3$ in DGM) reported previously by our group [38]. These results imply that the bulk structure and electrolyte components do not affect the sodium-insertion/desertion mechanism of the FeS. Thus, it cannot explain the electrochemical performance difference of FeS@N,S-C in the four electrolytes. Therefore, the interface might be the main reason.

The surface morphologies of cycled FeS@N,S-C electrodes in the four electrolytes are exhibited in Fig. S11, where a flat and compact electrode surface from $NaClO_4$ EC/PC electrolyte is presented. In contrast, the rougher electrode surface from $NaCF_3SO_3$ EC/PC electrolyte contains larger particles. On the electrode using $NaClO_4$ DGM electrolyte, an incompact surface with coarse stripes is observed clearly. The thicker flower-shaped agglomerates cover incompletely on the electrode in $NaCF_3SO_3$ DGM electrolyte, leading to a larger electrochemical impedance (Fig. S12). These results indicate that a more uniform SEI may form in $NaClO_4$ EC/PC electrolyte.

The SEI components are investigated by XPS spectra (Fig. 3a). In the C 1*s* spectrum from $NaClO_4$ EC/PC electrolyte, the C–C/C–H (284.8 eV), C-O (286.3 eV) and CO_3^{2-} (288.8 eV) peaks are attributed to common SEI components such as sodium alkyl carbonate or sodium carbonate (Na_2CO_3) and polyester [48,49]. While O 1*s* spectrum shows strong C=O (531.4 eV) and Na_2O (530.0 =-eV) peaks. The latter is mainly from the decomposition of ClO_4^- and carbonyl solvents [50,51], and weak NaF (684.2 eV) peak in F 1*s* spectrum is

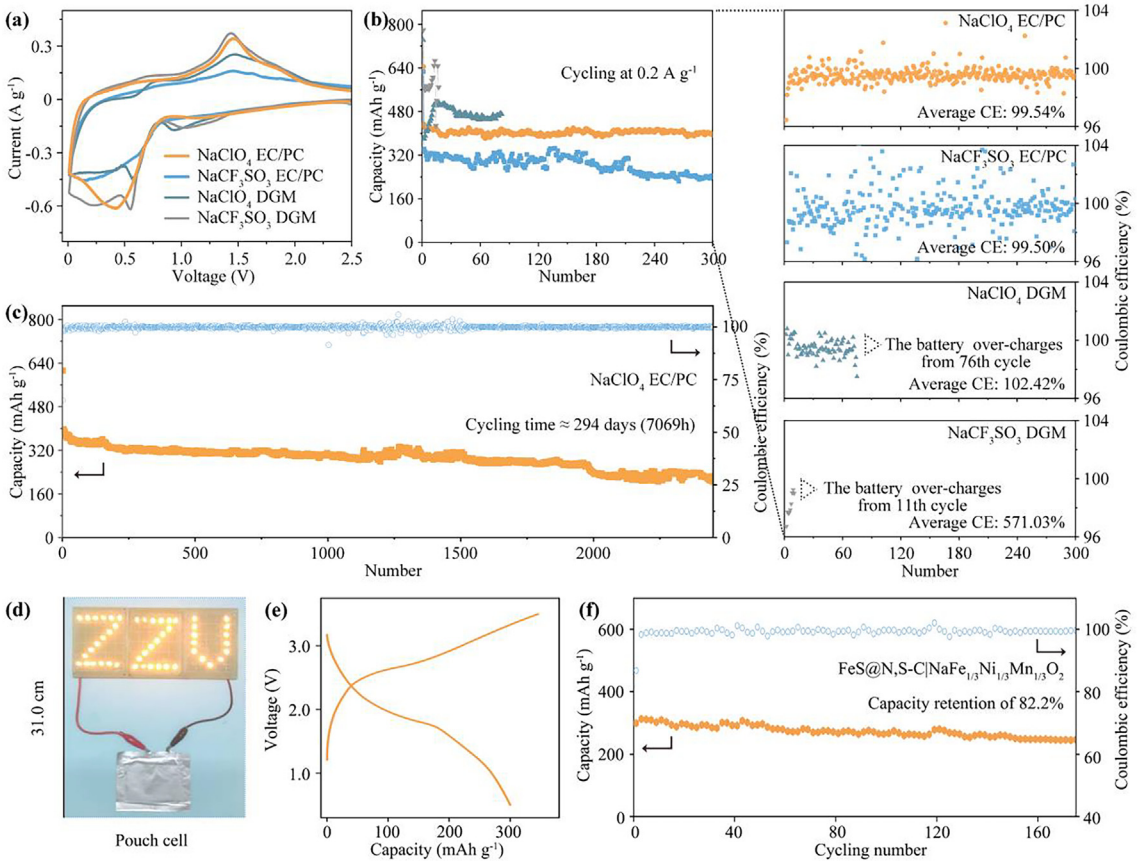

Fig. 2. Electrochemical performance of FeS@N,S-C electrode. (a) The initial cyclic voltammetry curves at 0.2 mV s^{-1} and (b) cycling performance at 0.2 A g^{-1} with the coulombic efficiency in various electrolytes, respectively. The average CE was obtained from the average value of CE from the second cycle. (c) Long-cycling performance at 0.2 A g^{-1} in $NaClO_4$ EC/PC electrolyte. (d) Digital photo, (e) charge–discharge curves and (f) cycling performance of FeS@N,S-C|$NaFe_{1/3}Ni_{1/3}Mn_{1/3}O_2$ pouch cell at 0.2 A g^{-1}.

derived from the FEC. In $NaCF_3SO_3$ EC/PC electrolyte, higher F-related peaks imply more serious electrolyte's decomposition from FEC and $NaCF_3SO_3$ salt [35], and C-O (532.5 eV) peak in O 1*s* spectrum indicates the polyester derived from solvents. In DGM-based electrolytes, the low-intensity peaks in C 1*s* spectra are ascribed to remarkable reduction stability of DGM, which maybe lead to the agglomeration of FEC's decomposition products on the electrode surfaces in DGM-based electrolytes, increasing the interfacial unevenness and impedance [52]. Meantime, low-content Na_2O (Fig. 3a) and NaCl (Fig. S13) in SEI may be powerless in enabling their compactness and robustness [53]. Furthermore, through Ar^+ etching treatment on FeS@N,S-C electrode surface in $NaClO_4$ EC/PC electrolyte (Fig. S14), the carbon content gradually decreases (Fig. 3b), which demonstrates the main distribution of organic components (C–C/C=C, C-O, $RCOO_2$) in the outer SEI. Inorganic species (NaCl and Na_2O) present the distribution through the whole depth, which render superior conductivity and compactness to SEI [54]. All these confirm the distinctive inorganic-rich SEI formed on FeS@N,S-C electrode in $NaClO_4$ EC/PC electrolyte.

TEM image demonstrates an integral SEI that fully covers FeS@N,S-C surface in $NaClO_4$ EC/PC electrolyte (Fig. 3c). Meantime, the discharged products remain fully embedded in the carbon matrix, demonstrating excellent structure stability of the electrode. Cryo-transmission electron microscopy (cryo-TEM) image further determines the susceptible nanostructure of SEI without beam damage [55]. A uniform SEI with a thickness of 35–45 nm, effectively preventing FeS@N,S-C electrode from sustained reductions of the electrolyte (Fig. 3d). The amorphous organics ensure a fully passivated interface. The large deep-colour areas on a nanometer scale filled with various lattice fringes correspond to high-content inorganic components, providing rapid Na^+ transfer paths across the SEI. Such a complex SEI layer with organic and inorganic species possesses both mechanical strength and toughness, stabilizing the electrode–electrolyte interface and maintaining its integrity during the long-term cycling [56]. Therefore, it should be the main reason for the excellent stability of FeS@N,S-C in $NaClO_4$ EC/PC electrolyte.

The structure and interface evolution of FeS@N,S-C electrodes in $NaClO_4$ EC/PC electrolyte after long-lasting cycling were also investigated. The electrode after 50 cycles still displays obvious bulk structures, in which abundant internal pores help maintain the electrode's structural stability during the repeated (de)sodiation process (Fig. S15). While the prominent element peaks in SEI keep relatively steady at charged 2.5 V of the initial cycle, indicating little re-consumption of the electrolyte (Fig. S16). After 290-day cycling, the interface remains stable without an explosive increase in peak intensities (Fig. S17). Meantime, the clearer and flatter bulk electrode surface in $NaClO_4$ EC/PC electrolyte implies a more stable SEI (Fig. S18) [57]. In contrast, rougher surfaces contain numerous aggregates in the electrodes of the other three electrolytes, indicating severely interfacial side reactions, which are fundamentally associated with poor SEI [33].

The effect of electrode surface on SEI formation is revealed via optimized Na^+-solvation structures in the four electrolytes by DFT calculation. For simplification, FEC additive in electrolytes is ignored. The negative charge (red) is mainly localized on the O of C=O group and salt anions, respectively (Fig. 4a). Owing to the larger volume of $CF_3SO_3^-$ and relatively low electron density of DGM,

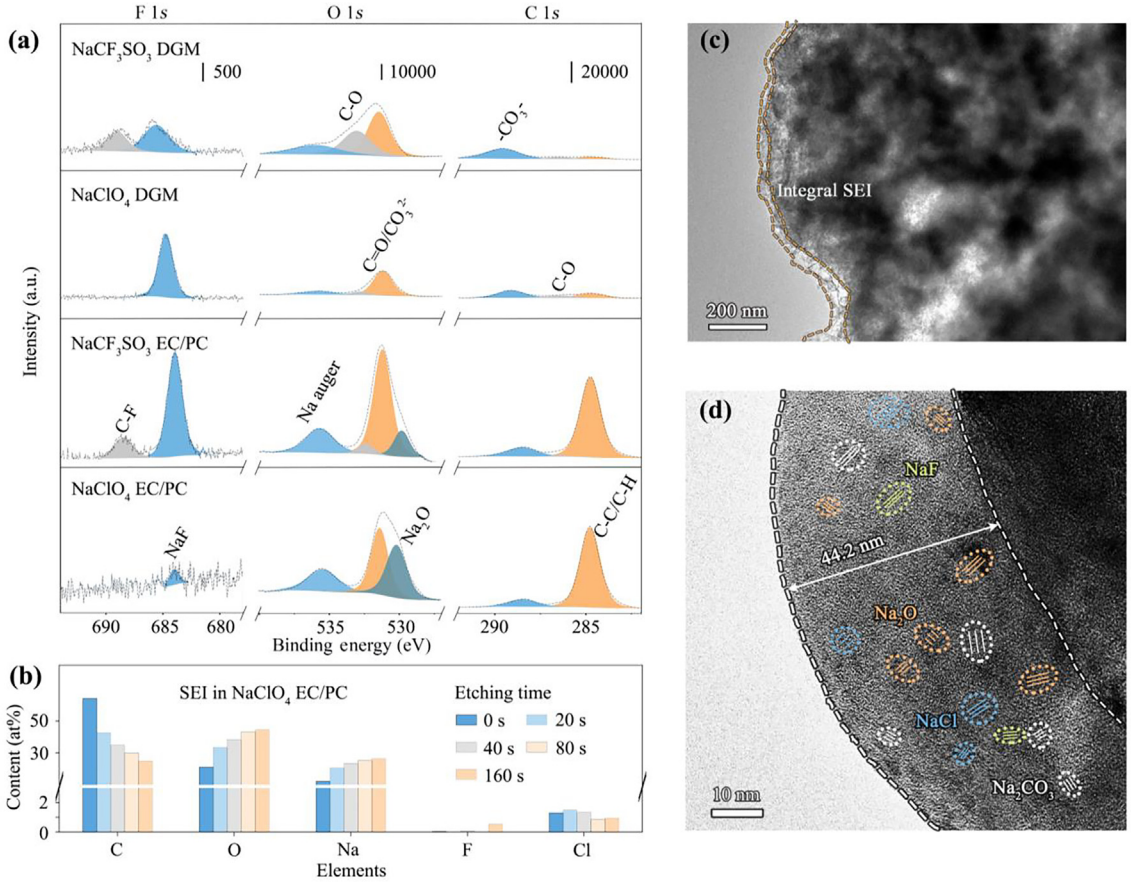

Fig. 3. Study on the SEI of FeS@N,S-C electrodes at discharged 0.01 V upon the initial cycle. (a) High-resolution XPS spectra in various electrolytes: C 1*s*, O 1*s* and F 1*s*. (b) Element distributions in-depth tested by XPS etching. (c) TEM and (d) cryo-TEM images in $NaClO_4$ EC/PC electrolyte.

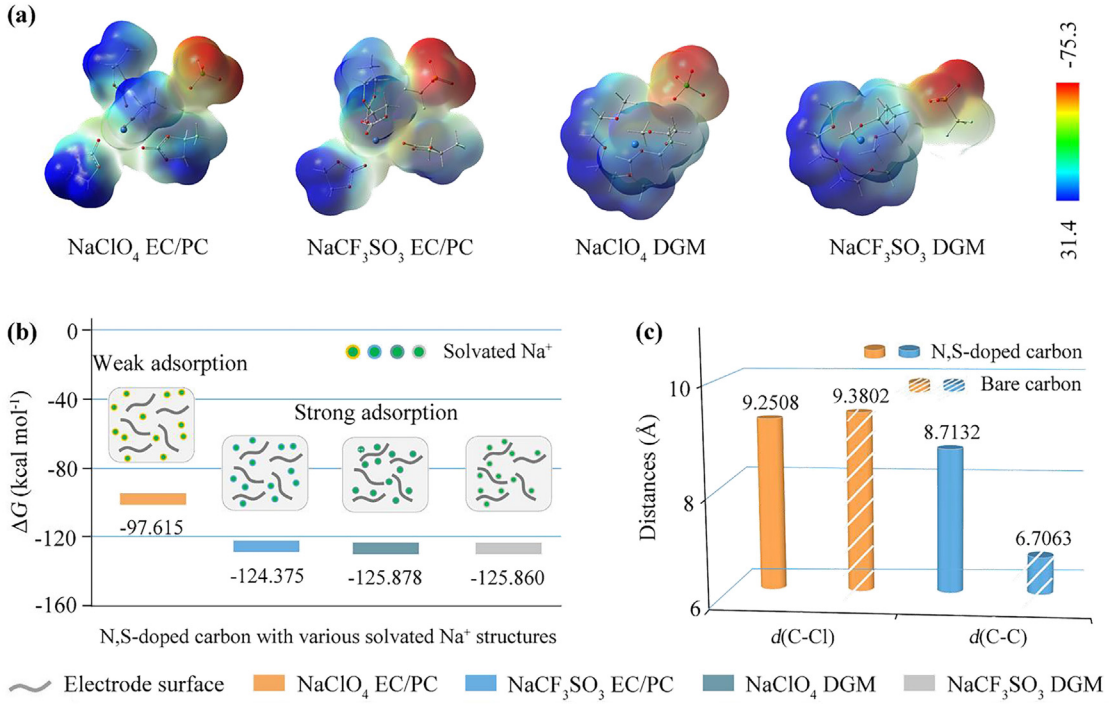

Fig. 4. DFT calculations on electrolytes' electrochemistry on electrode surfaces. (a) Electrostatic potential maps of four Na^+-solvation structures. The scale unit of electronic static potential is kcal mol^{-1}. (b) ΔG values after compositing N,S-doped carbon structures with four Na^+-solvation structures, respectively. (c) The lowest distance between N, S-doped/pure carbon structures and anions in $NaClO_4$ EC/PC (C-Cl bond) and $NaCF_3SO_3$ EC/PC (C–C bond) electrolytes, respectively.

the higher electron density is presented in ClO_4^- and EC/PC molecules. When put Na^+-solvation structures and N,S-doped carbon structure into a simulating electrolyte environment, larger $d_{C\text{-}Na}$ value (the lowest distance between carbon structures and Na^+ ion) is presented in $NaClO_4$ EC/PC compared with others (Fig. S19), demonstrating the weaker adsorption between N,S-doped carbon and solvated Na^+. The reduced ΔG indicate an energetically favourable process (Fig. 4b). Meantime, larger absolute values of ΔG also imply stronger adsorption on the electrode surface, which will further deteriorate the Na^+ transport, leading to uneven distribution of electrons/ions, and finally controlling the generated SEI with poor integrity and compactness [44]. Further calculations about pure carbon structure show a lower $d_{C\text{-}Na}$ value in $NaClO_4$ EC/PC but a higher $d_{C\text{-}Na}$ value in the other three electrolytes (Fig. S20). It implies that, after the N,S-doping into carbon surface, strong repulsive interaction in $NaClO_4$ EC/PC and attractive interaction in other three electrolytes are produced at electrode–electrolyte interfaces. Such opposite interaction will cause different interfacial effects. Concretely, solvated Na^+ in $NaClO_4$ EC/PC electrolyte is more difficult to be trapped by N,S-doped carbon surface, giving an advantage for ClO_4^- anions during the competitive adsorption process. While in the other three electrolytes, solvated Na^+ is accumulated gradually on the surface before reaching the decomposition voltage of the electrolyte components. Once the electrode reaches an appropriate negative potential, excess solvated Na^+ are easy to dissociation and subsequently evolve into the solvent-rich precursor of SEI. However, these adsorptions cannot increase the reduction activity of DGM, making the decomposition products of FEC constitute the main components of SEI in DGM-based electrolytes. Furthermore, the distance between ClO_4^- and N,S-doped carbon (C-Cl) decreases slightly in $NaClO_4$ EC/PC compared with the value between ClO_4^- and pure carbon, while $CF_3SO_3^-$ are alienated from the N,S-doped carbon (C–C) (Fig. 4c), demonstrating that N,S-doping guide ClO_4^- to preferentially take part in the inner Helmholtz plane (IHP) and reduce to form the SEI subsequently [58]. These firmly support the ability of the electrode's surface properties to tune the interfacial behavior of electrolytes. N,S-doped carbon surface is favourable to alienate solvated Na^+ but endear the adsorption to ClO_4^- anion in the IHP, enabling a distinctive inorganic-rich SEI (NaCl, Na_2O) for FeS@N, S-C electrode in $NaClO_4$ EC/PC electrolyte.

To further confirm the interfacial effect induced by N,S-doping, other examples, including FeS@C, CoS@N,S-C and CoS@C, carbon materials (N,S-doped carbon (NSC) and bare carbon (BC)) are prepared based on similar preparation processes (See the Experimental section). Apparently, the superiority in CE are presented in N,S-doped carbon composite electrodes (FeS@N,S-C, NSC, CoS@N,S-C) (Fig. 5a–c and Fig. S21). In contrast, all doping-free electrodes (FeS@C, BC, CoS@C) display lower and unexpectedly unstable CE, demonstrating the continuous electrolyte decomposition induced by unstable SEI [47]. On the other hand, N,S-doped carbon defects inevitably trap Na^+ during the desolvation process and generate a more uneven electric field, resulting in more electrolyte's decomposition and a thicker SEI [59], which is also demonstrated by TEM images (Fig. S22a–d). Due to the influence of complex preparation factors, it is difficult to obtain the optimal N,S-doping content in FeS@N,S-C electrodes enabling balanced electrode–electrolyte interaction and electrolyte decomposition (Fig. S23 and Fig. S24). Even so, more inorganic components (NaCl, Na_2O) derived from ClO_4^- anion are observed in the SEI of FeS@N,S-C electrode, enabling an obviously smaller interfacial resistance (R_{SEI}) value (Fig. S22e–g and Table S2). According to the Arrhenius formula, the interfacial resistance (R_{SEI})-derived E_a values are calculated to be 56.02 kJ mol^{-1} (for FeS@N,S-C) and 65.13 kJ mol^{-1} (for FeS@C), respectively [39]. This indicates that the uniform SEI on FeS@N,S-C electrode with more rich inorganics enables Na^+ lower activation energy for interfacial transfer and faster dynamic behavior in passing through the SEI, which highlights the key role of N,S-doping carbon surface in facilitating the formation of highly robust SEI (Fig. 5d).

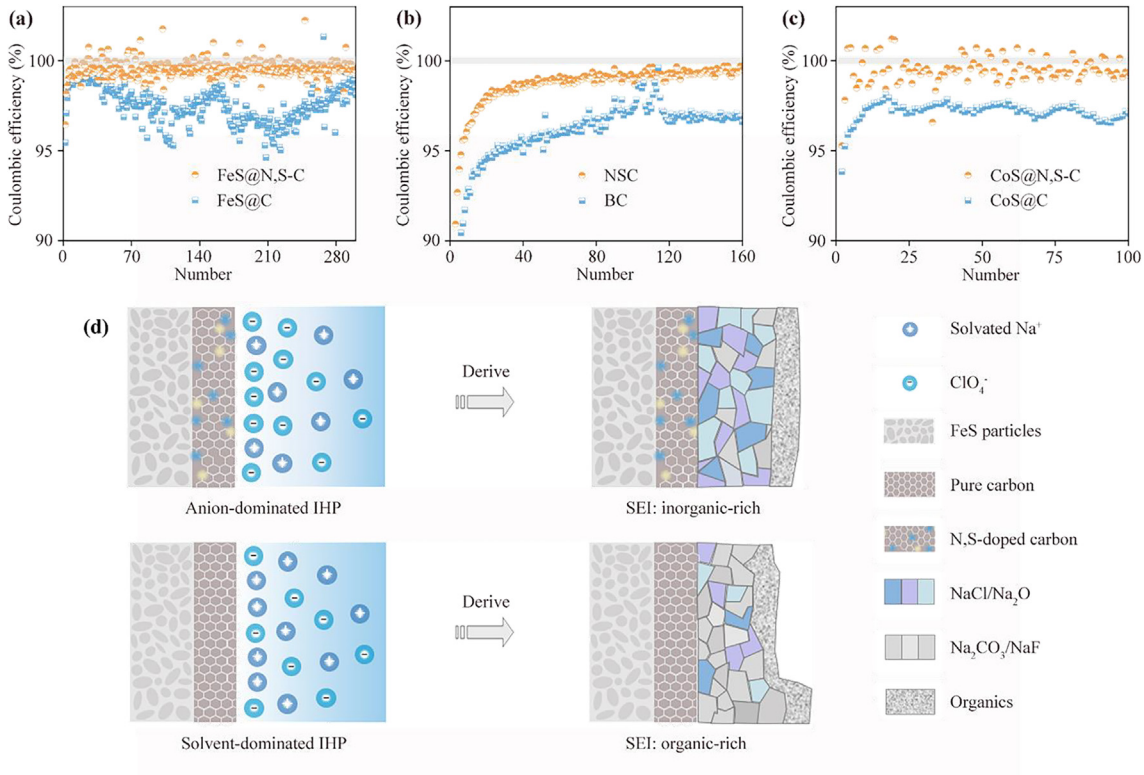

Fig. 5. Extended confirmations and schematic of interfacial effect. CE of (a) FeS@N,S-C and FeS@C electrodes, (b) NSC and BC electrodes, (c) CoS@N,S-C and CoS@C electrodes at 0.2 A g^{-1} in $NaClO_4$ EC/PC electrolyte, respectively. (d) Schematic diagram of electrode's electronic properties influencing SEI formation.

3. Conclusion

In summary, FeS@N,S-C with rich void space in bulk is synthesized through a facile freeze-drying process and subsequent annealed step. When applied in SIBs as the anode, FeS@N,S-C shows comfortable compatibility and ultra-long lifespan (294 days) in the ester-based electrolyte ($NaClO_4$ EC/PC), while poor cycling stability is presented in other electrolytes ($NaCF_3SO_3$ EC/PC, $NaClO_4$ DGM and $NaCF_3SO_3$ DGM). Physical characterization results indicate that the as-synthesized FeS@N,S-C contains enriching element doping of nitrogen and sulfur with extra pair of electrons, resulting in the enrichment of electrons on the surface. Unlike the cases of undoped carbon surfaces, the repulsive interaction is produced in the Na^+-solvation structure of $NaClO_4$ EC/PC with the higher electronic cloud density, promoting the formation of inorganic-rich SEI that enables the improvement of interfacial compatibility. While for Na^+-solvation structure of other electrolytes with lower electronic cloud densities, stronger attractive interaction is formed and causes the formation of rougher and uneven SEI, accounting for the interfacial instability between anode and electrolytes. The unusual results in ester-based and ether-based electrolytes can be ascribed to the distinctive electrode–electrolyte interactions originating from the strong electronegativity on the electrode surface. We have emphasized the importance of electrode surface properties in interfacial compatibility. With the regulation of the electrode–electrolyte interaction reasonably, a stable interface can be constructed via chemical modification on electrode surface using doped-atoms with high electronegativity. As a result, as-assembled pouch cells can achieve excellent cycling stability (capacity retention of 82.2% after 170 cycles at 0.2 A g^{-1}) without the pre-activation process of electrodes in their preferable electrolytes. Therefore, this work not only provides novel understandings about the effect of anode material's surface properties on the formation of SEI but also sheds light on improving the electrode–electrolyte interfacial compatibility in rechargeable batteries.

Declaration of Competing Interest

The authors declare that they have no known competing financial interests or personal relationships that could have appeared to influence the work reported in this paper.

Acknowledgments

This work was supported by the National Natural Science Foundation of China (U1804129, 21771164), the Program for Young Scholar of Changjiang Scholars, Zhongyuan Youth Talent Support Program of Henan Province, Zhengzhou University Youth Innovation Program. We acknowledge the National Supercomputing Centre in Zhengzhou and Henan Province Supercomputing Centre for the computational support. And we are grateful for testing support from Modern Analysis and Gene Sequencing Centre of Zhengzhou University and Shanghai Synchrotron Radiation Facility (SSRF), Shanghai, China.

Appendix A. Supplementary data

Supplementary data to this article can be found online at https://doi.org/10.1016/j.jechem.2021.11.033.

References

[1] C. Zhao, Q. Wang, Z. Yao, J. Wang, B. Sánchez-Lengeling, F. Ding, X. Qi, Y. Lu, X. Bai, B. Li, H. Li, A. Aspuru-Guzik, X. Huang, C. Delmas, M. Wagemaker, L. Chen, Y. Hu, Science 370 (2020) 708–711.
[2] Y. Xiang, G. Zheng, Z. Liang, Y. Jin, X. Liu, S. Chen, K. Zhou, J. Zhu, M. Lin, H. He, J. Wan, S. Yu, G. Zhong, R. Fu, Y. Li, Y. Yang, Nat. Nanotechnol. 15 (2020) 883–890.
[3] K. Song, J. Liu, H. Dai, Y. Zhao, S. Sun, J. Zhang, C. Qin, P. Yan, F. Guo, C. Wang, Y. Cao, S. Li, W. Chen, Chem 7 (2021) 2684–2694.
[4] Y. Huang, L. Zhao, L. Li, M. Xie, F. Wu, R. Chen, Adv. Mater. 31 (2019) 1808393.
[5] H. Liang, Z. Gu, X. Zhao, J. Guo, J. Yang, W. Li, B. Li, Z. Liu, W. Li, X. Wu, Angew. Chemie - Int. Ed. (2021), https://doi.org/10.1002/anie.202112550.
[6] G. Yao, X. Zhang, Y. Yan, J. Zhang, K. Song, J. Shi, L. Mi, J. Zheng, X. Feng, W. Chen, J. Energy Chem. 50 (2020) 387–394.
[7] Z. Zhang, Y. Du, Q. Wang, J. Xu, Y. Zhou, J. Bao, J. Shen, X. Zhou, Angew. Chemie - Int. Ed. 59 (2020) 17504–17510.
[8] B. Peng, Z. Sun, L. Zhao, J. Li, G. Zhang, Energy Storage Mater. 35 (2021) 620–629.
[9] L. Yang, Q. Liu, M. Wan, J. Peng, Y. Luo, H. Zhang, J. Ren, L. Xue, W. Zhang, J. Power Sources 448 (2020) 227421.
[10] J. Xu, E. Gu, Z. Zhang, Z. Xu, Y. Xu, Y. Du, X. Zhu, X. Zhou, J. Colloid Interf. Sci. 567 (2020) 84–91.
[11] Y. Xu, Y. Du, Z. Yi, Z. Zhang, C. Lai, J. Liao, X. Zhou, J. Energy Chem. 58 (2021) 593–601.
[12] R. Dong, L. Zheng, Y. Bai, Q. Ni, Y. Li, F. Wu, H. Ren, C. Wu, Adv. Mater. 33 (2021) 2008810.
[13] M. Rybarczyk, Y. Li, M. Qiao, Y. Hu, M. Titirici, M. Lieder, J. Energy Chem. 29 (2019) 17–22.
[14] W. Chen, X. Zhang, L. Mi, C. Liu, J. Zhang, S. Cui, X. Feng, Y. Cao, C. Shen, Adv. Mater. 31 (2019) 1–9.
[15] P. Le, T. Vo, H. Pan, Y. Jin, Y. He, X. Cao, H. Nguyen, M. Engelhard, C. Wang, J. Xiao, J. Zhang, Adv. Funct. Mater. 30 (2020) 2001151.
[16] J. Ming, Z. Cao, Q. Li, W. Wahyudi, W. Wang, L. Cavallo, K. Park, Y. Sun, H. Alshareef, ACS Energy Lett. 4 (2019) 1584–1593.
[17] L. Cao, D. Li, T. Pollard, T. Deng, B. Zhang, C. Yang, L. Chen, J. Vatamanu, E. Hu, M. Hourwitz, L. Ma, M. Ding, Q. Li, S. Hou, K. Gaskell, J. Fourkas, X. Yang, K. Xu, O. Borodin, C. Wang, Nat. Nanotechnol. 16 (2021) 902–910.
[18] K. Doi, Y. Yamada, M. Okoshi, J. Ono, C. Chou, H. Nakai, A. Yamada, Angew. Chemie - Int. Ed. 58 (2019) 8024–8028.
[19] X. Chen, X. Shen, T. Hou, R. Zhang, H. Peng, Q. Zhang, Chem 6 (2020) 2242–2256.
[20] Y. Yamada, J. Wang, S. Ko, E. Watanabe, A. Yamada, Nat. Energy 4 (2019) 269–280.
[21] R. Dugas, A. Ponrouch, G. Gachot, R. David, M. Palacin, J. Tarascon, J. Electrochem. Soc. 163 (2016) A2333–A2339.
[22] J. Shi, L. Ding, Y. Wan, L. Mi, L. Chen, D. Yang, Y. Hu, W. Chen, J. Energy Chem. 57 (2021) 650–655.
[23] N. Takenaka, A. Bouibes, Y. Yamada, M. Nagaoka, A. Yamada, Adv. Mater. 33 (2021) 2100574.
[24] Y. Li, M. Liu, X. Feng, Y. Li, F. Wu, Y. Bai, C. Wu, ACS Energy Lett. 6 (2021) 3307–3320.
[25] W. Song, E. Scholtis, P. Sherrell, D. Tsang, J. Ngiam, J. Lischner, S. Fearn, V. Bemmer, C. Mattevi, N. Klein, F. Xie, D. Riley, Energy Environ. Sci. 13 (2020) 4977–4989.
[26] C. Yan, L. Jiang, Y. Yao, Y. Lu, J. Huang, Q. Zhang, Angew. Chemie - Int. Ed. 60 (2021) 8521–8525.
[27] T. Li, X. Zhang, P. Shi, Q. Zhang, Joule 3 (2019) 2647–2661.
[28] Z. Li, Y. Zhang, X. Li, F. Gu, L. Zhang, H. Liu, Q. Xia, Q. Li, W. Ye, C. Ge, H. Li, H. Hu, S. Li, Y. Long, S. Yan, G. Miao, Q. Li, J. Am. Chem. Soc. 143 (2021) 12800–12808.
[29] L. Chen, K. Song, J. Shi, J. Zhang, L. Mi, W. Chen, C. Liu, C. Shen, Sci. China Mater. 64 (2021) 105–114.
[30] Z. Hu, Z. Zhu, F. Cheng, K. Zhang, J. Wang, C. Chen, J. Chen, Energy Environ. Sci. 8 (2015) 1309–1316.
[31] Y. Wan, K. Song, W. Chen, C. Qin, X. Zhang, J. Zhang, H. Dai, Z. Hu, P. Yan, C. Liu, S. Sun, S. Chou, C. Shen, Angew. Chemie - Int. Ed. 60 (2021) 11481–11486.
[32] Q. Liu, Z. Hu, C. Zou, H. Jin, S. Wang, L. Li, Cell Reports Phys. Sci. 2 (2021) 100551.
[33] X. Liu, B. Xiao, A. Daali, X. Zhou, Z. Yu, X. Li, Y. Liu, L. Yin, Z. Yang, C. Zhao, L. Zhu, Y. Ren, L. Cheng, S. Ahmed, Z. Chen, X. Li, G. Xu, K. Amine, ACS Energy Lett. 6 (2021) 547–556.
[34] C. Zhang, L. Dong, N. Zheng, H. Zhu, C. Wu, F. Zhao, W. Liu, Energy Storage Mater. 37 (2021) 296–305.
[35] X. Hu, Y. Liu, J. Chen, J. Jia, H. Zhan, Z. Wen, J. Mater. Chem. A 7 (2019) 1138–1148.
[36] D. Li, Y. Sun, S. Chen, J. Yao, Y. Zhang, Y. Xia, D. Yang, ACS Appl. Mater. Inter. 10 (2018) 17175–17182.
[37] X. Ge, S. Liu, M. Qiao, Y. Du, Y. Li, J. Bao, X. Zhou, Angew. Chemie - Int. Ed. 58 (2019) 14578–14583.
[38] D. Yang, W. Chen, X. Zhang, L. Mi, C. Liu, L. Chen, X. Guan, Y. Cao, C. Shen, J. Mater. Chem. A 7 (2019) 19709–19718.
[39] X. Wang, J. Shi, L. Mi, Y. Zhai, J. Zhang, X. Feng, Z. Wu, W. Chen, Rare Met. 39 (2020) 1053–1062.
[40] F. Wang, G. Li, X. Meng, Y. Li, Q. Gao, Y. Xu, W. Cui, Inorg. Chem. Front. 5 (2018) 2462–2471.
[41] Y. Wang, J. Yang, S. Chou, H. Liu, W. Zhang, D. Zhao, S. Dou, Nat. Commun. 6 (2015) 1–9.
[42] A. Jin, S. Yu, J. Park, S. Kang, M. Kim, T. Jeon, J. Mun, Y. Sung, Nano Res. 12 (2019) 2609–2613.
[43] M. Dahbi, T. Nakano, N. Yabuuchi, S. Fujimura, K. Chihara, K. Kubota, J. Son, Y. Cui, H. Oji, S. Komaba, ChemElectroChem 3 (2016) 1856–1867.

[44] Y. Zhen, R. Sa, K. Zhou, L. Ding, Y. Chen, S. Mathur, Z. Hong, Nano Energy 74 (2020) 104895.
[45] C. Bao, B. Wang, P. Liu, H. Wu, Y. Zhou, D. Wang, H. Liu, S. Dou, Adv. Funct. Mater. 30 (2020) 1–27.
[46] J. Xiao, Q. Li, Y. Bi, M. Cai, B. Dunn, T. Glossmann, J. Liu, T. Osaka, R. Sugiura, B. Wu, J. Yang, J. Zhang, M. Whittingham, Nat. Energy 5 (2020) 561–568.
[47] M. Schulze, N. Neale, ACS Energy Lett. 6 (2021) 1082–1086.
[48] Y. Xu, H. Sun, C. Ma, J. Gai, Y. Wan, W. Chen, Chin. J. Chem. Eng. (2021), https://doi.org/10.1016/j.cjche.2021.08.020.
[49] Z. Wang, H. Yang, Y. Liu, Y. Bai, G. Chen, Y. Li, X. Wang, H. Xu, C. Wu, J. Lu, Small 16 (2020) 2003268.
[50] G. Eshetu, T. Diemant, M. Hekmatfar, S. Grugeon, R. Behm, S. Laruelle, M. Armand, S. Passerini, Nano Energy 55 (2019) 327–340.
[51] L. Kuo, A. Moradabadi, H. Huang, B. Hwang, P. Kaghazchi, J. Power Sources 341 (2017) 107–113.
[52] A. Bouibes, N. Takenaka, T. Fujie, K. Kubota, S. Komaba, M. Nagaoka, ACS Appl. Mater. Inter. 10 (2018) 28525–28532.
[53] C. Yan, R. Xu, Y. Xiao, J. Ding, L. Xu, B. Li, J. Huang, Adv. Funct. Mater. 30 (2020) 1909887.
[54] J. Zhang, K. Song, L. Mi, C. Liu, X. Feng, J. Zhang, W. Chen, C. Shen, J. Phys. Chem. Lett. 11 (2020) 1435–1442.
[55] J. Huang, X. Guo, X. Du, X. Lin, J. Huang, H. Tan, Y. Zhu, B. Zhang, Energy Environ. Sci. 12 (2019) 1550–1557.
[56] X. Shen, R. Zhang, X. Chen, X. Cheng, X. Li, Q. Zhang, Adv. Energy Mater. 10 (2020) 1903645.
[57] X. Hu, E. Matios, Y. Zhang, C. Wang, J. Luo, W. Li, Angew. Chemie - Int. Ed. 60 (2021) 5978–5983.
[58] C. Yan, H. Li, X. Chen, X. Zhang, X. Cheng, R. Xu, J. Huang, Q. Zhang, J. Am. Chem. Soc. 141 (2019) 9422–9429.
[59] H. He, D. Sun, Y. Tang, H. Wang, M. Shao, Energy Storage Mater. 23 (2019) 233–251.